Table 3. Observation log.

KIG	Exp. time [s]	Date	Filter SDSS	*FWHM* [arcsec]	ZP mag
264	1800	9	*g*	1.″2	22.83 ± 0.03
	660	10	*r*	1.″1	23.18 ± 0.05
378	600	15	*g*	1.″3	21.81 ± 0.02
	540	15	*r*	1.″0	21.94 ± 0.02
412	1500	11	*g*	1.″3	23.01 ± 0.03
	2340	13	*r*	1.″0	21.64 ± 0.04
481	2100	13	*g*	2.″0	22.62 ± 0.04
	1080	13	*r*	2.″0	22.44 ± 0.02
490	1500	14	*g*	1.″3	22.98 ± 0.05
	1260	14	*r*	1.″0	22.27 ± 0.01
517	2700	9, 15	*g*	1.″2	22.27 ± 0.12
	2340	9, 15	*r*	1.″0	21.64 ± 0.09
578	2400	15	*g*	1.″2	22.56 ± 0.11
	1440	15	*r*	1.″2	22.15 ± 0.01
595	3000	11	*g*	1.″0	22.65 ± 0.05
	1800	11	*r*	1.″1	22.46 ± 0.06
599	1800	9	*g*	1.″6	22.69 ± 0.06
	1650	9	*r*	1.″1	22.46 ± 0.06
620	2400	13	*g*	2.″0	22.44 ± 0.02
	1440	13	*r*	1.″8	22.09 ± 0.01
636	2400	15	*g*	1.″1	22.50 ± 0.04
	1440	15	*r*	1.″4	22.17 ± 0.02
637	1800	14	*g*	1.″2	22.78 ± 0.01
	1440	14	*r*	1.″4	22.11 ± 0.01
644	1800	10	*g*	1.″3	22.85 ± 0.03
	1800	10	*r*	1.″3	21.92 ± 0.02
670	2100	13	*g*	1.″8	22.62 ± 0.04
	1800	13	*r*	1.″6	22.45 ± 0.01
685	2400	14	*g*	0.″9	22.27 ± 0.03
	1440	14	*r*	1.″2	22.12 ± 0.04
705	1510	9	*g*	1.″3	22.50 ± 0.05
	1200	9	*r*	1.″0	21.87 ± 0.02
722	1800	13	*g*	2.″6	22.74 ± 0.07
	900	14	*r*	0.″8	22.65 ± 0.04
732	3150	11	*g*	1.″5	22.41 ± 0.02
	1800	11	*r*	1.″3	21.80 ± 0.01
733	3000	15	*g*	1.″2	22.24 ± 0.06
	1800	15	*r*	1.″1	21.68 ± 0.04
841	1500	10	*g*	1.″0	23.04 ± 0.01
	1800	10	*r*	1.″1	21.92 ± 0.03

Notes. We report the total exposure time in Col. 2. Galaxies were observed in April 2018: the observing date is given in Col. 3. The filter and average Gaussian FWHM of stars nearby the galaxy, measured on the co-added images using the `IRAF` task `IMEXAMINE`, are reported in Cols. 4 and 5 respectively (see Sect. 3). The adopted ZP are provided in Col. 6.

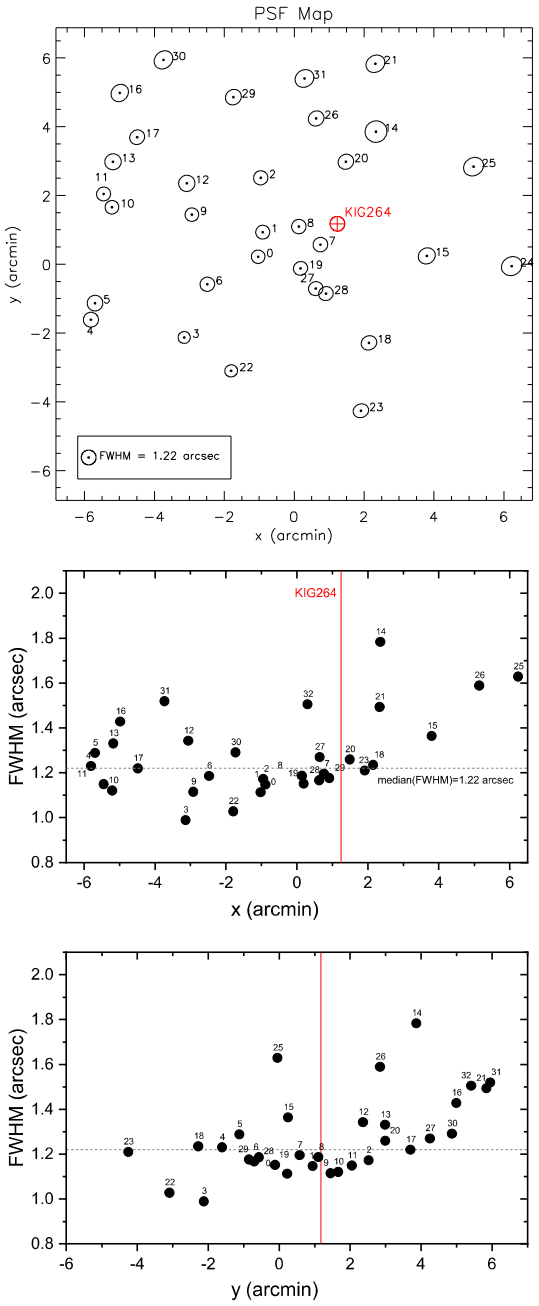

Fig. 3. *Top panel:* 2D map of the PSF FWHM variation across the *g* -band FOV of KIG 264. *Middle panel:* FWHM measured along the *x*-axis (RA) and along the *y*-axis (Decl., bottom panel) of this frame. The vertical red line marks the position of KIG 264.

3.3. Data analysis

Our scientific aim is twofold: to unveil fine structures, and to quantitatively refine the galaxy morphology given in Table 1. The sample is composed of Es and S0s to about the same portions. However, the three classifications considered in Table 1 often differ significantly, as shown in Fig. 1. To ascertain the presence of a disc is very valuable information about the role of *dissipative processes* in the ETGs evolution. We are aware that the photometric evidence is, however, a necessary but not sufficient condition (see e.g. Meert et al. 2015; Costantin et al. 2018, for an ample discussion) to determine the presence of a kinematical disc.

We remark that our purpose does not consist of introducing additional functions to possibly best fit *regular* features (e.g. analytic functions to mimic a bar, rings etc., as e.g. in `GALFIT` or `IMFIT` approaches). On the one hand, the fine structure we aim to reveal, such as shells, ripples, and tails, are often if not always irregular. Fine structures should be visible in the image itself. Fitted models are intended to enhance fine structures when they are subtracted from the original image. On the other hand, the visual classification in Table 1 reports only few iETGs with a

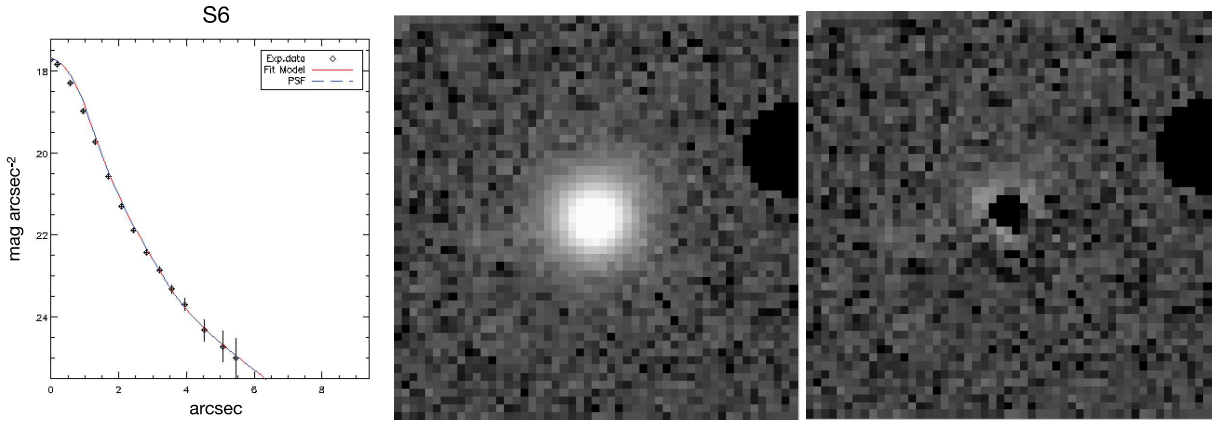

Fig. 4. PSF in KIG 264 in the g band. The 2D PSF is best fitted with a composite model (solid line) combining three Gaussians plus an exponential. The adopted PSF has been generated from a set of stars (star 6 is shown) close to the galaxy. The seeing correction is extrapolated up to the galaxy outskirts (see the discussion in Rampazzo et al. 2019, and references therein). A masked star is visible on the NW side of the field.

ring or bar, or mixed AB types in the Buta et al. (2019) classification. In addition, the galaxies that are acknowledged to possess these features are not necessarily the same in the three classifications presented in Table 1. Only KIG 264 is considered barred by Buta et al. (2019), while KIG 264, KIG 620, and KIG 636 for HyperLeda are barred S0s. Buta et al. (2019) considered KIG 620, KIG 636 and KIG 733 as mixed AB type. Some of these galaxies have an inner ring. Only KIG 733 for Buta et al. (2019) and KIG 599 and KIG 644 for HyperLeda possess outer rings.

To conclude, we are aware that bars and inner rings introduce an erroneous evaluation of the bulge parameters if they are not considered in the fit. Meert et al. (2015) remarked that the presence of a bar affects the fitting by changing the ellipticity and Sérsic index of the bulge component in their two-component models. However, the classifications severely differ in our case, so that the presence of bar and rings needs to be carefully determined by our surface photometry. Our results are described in detail in Sect. 4.2.

We used two models to best fit the galaxy light profile. We best fit a single Sérsic law (Sérsic 1968), which is intended to represent Es (see e.g. Ho et al. 2011; Li et al. 2011, and reference therein) and a classic bulge (de Vaucouleurs 1953) plus an exponential disc (Freeman 1970), labelled B+D hereafter, for disc galaxies. The Sérsic law exponent was left free to vary up to $n \leq 10$ in the single Sérsic fit (the values $n = 1$ and $n = 4$, the Freeman and de Vaucouleurs laws, respectively, are special cases). The selection of the B+D model is justified by the following consideration that takes into account that our range of morphological type is $-5 \leq T \leq 0$ according to Fernandez-Lorenzo et al. (2012), which we used for sample selection. Large surveys based on SDSS, which used automated decomposition algorithms, widely debated the biases introduced in the galaxy final structural parameters by fitting the light profiles using different models, mostly in connection with image resolution and galaxies with $B/T \leq 0.5$ (see e.g. Gaditti 2009; Simard et al. 2011; Meert et al. 2015). Our targets are nearby (see Table 1), extended, and relatively bright galaxies (see Table 2). The galaxy light is dominated by the bulge (the average is $\langle B/T \rangle = 0.67$), as discussed in Sect. 4. Meert et al. (2015) showed that B/T, bulge radius, and bulge Sérsic index all decrease with increasing T-type. The median bulge Sérsic index in their fit of a Sérsic plus exponential disc for the earliest T-types ($-5 \leq T \leq 0$) is approximately 5.0 ± 1.5 (see their Fig. 23), which is fully consistent with our use of a de Vaucouleurs law. Their median B/T decreases from 0.8 to 0.5 over the same range as in our case (see our Sect. 4).

The fit quality, as described in Uslenghi & Falomo (2011), was estimated by minimising the χ^2. In AIDA, the minimised χ^2 is defined as

$$\chi^2 = \sum_y \sum_x \frac{(\mathrm{flux}_{x,y} - \mathrm{Model})^2}{\sigma^2_{x,y}} \mathrm{Mask}_{\mathrm{x,y}} \quad (1)$$

The masked pixels are excluded from the fit. The weighted model is computed defining $\sigma_{x,y}$ as the sum in quadrature of three distinct components with different dependence on the signal level,

$$\sigma_{x,y} = \sqrt[2]{C^2 + SY \times (\sqrt[2]{\mathrm{Flux}_{x,y}})^2 + (\alpha \times \mathrm{Flux}_{x,y})^2}. \quad (2)$$

C, SY, and α can be provided either by the user or they can be computed by AIDA based on readout noise and gain. If $SY = \alpha = 0$, the fit is unweighted. In general, C describes the constant component of the noise, which is independent of the signal (in the ideal case, it coincides with the readout noise, without sky background), SY describes the component proportional to the square root of the signal (shot noise, in this case, SY is related to the conversion factor Ke-/ADU), and α represents the fixed pattern noise. We selected the weighted fit in both Sérsic and B+D models, tailored to the 4KCCD.

Meert et al. (2015) noted that when multiple components are fitted, a significant second component may only indicate substantial departure from a single-component profile rather than the presence of a physically meaningful second component. They quoted as examples Gonzalez et al. (2005), Donzelli et al. (2011), and Huang et al. (2013), who fitted multiple components to ellipticals (E) and bright cluster galaxies without necessarily claiming the existence of additional physically distinct components. Our data set is deeper than the SDSS data set, and this significantly affects the model selection. The single Sérsic fit often tends to overestimate the galaxy luminosity at low surface brightness levels, for instance, also when fine structures are present. The effect on the magnitude estimate is weak, but the B+D model is statistically better by far (even by eye) in describing the galaxy light profile for most of our iETGs. The images in g and r bands of the iETGs in our sample and a summary of the analysis performed are collected in Fig. 5 and in Appendix A.

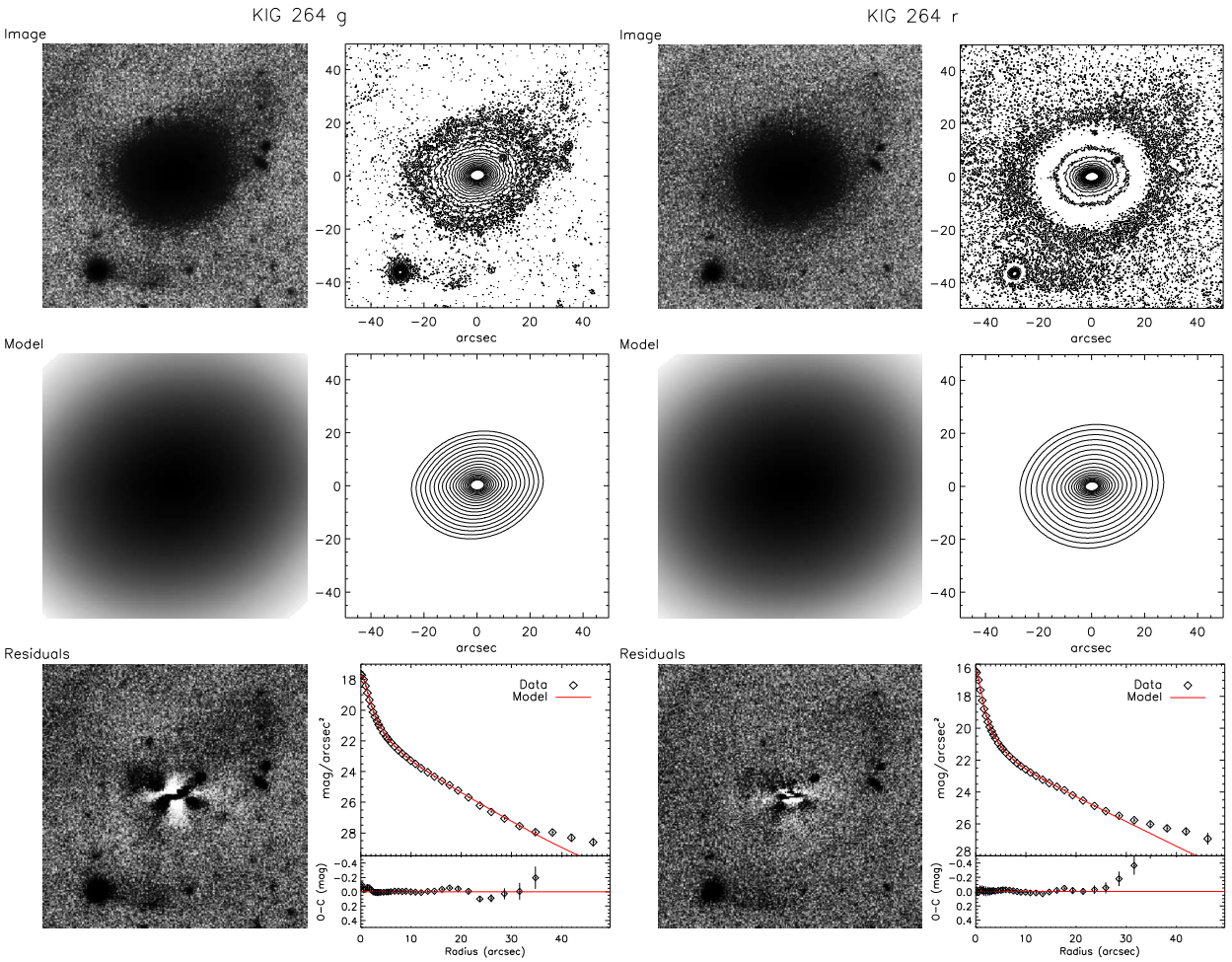

Fig. 5. Summary of the $g-$ (*left panels*) and $r-$ (*right panels*) band surface photometry of KIG 264. The adopted masks of the foreground and background objects are not shown. North is up, and east is to the left. The right panels provide from top to bottom (*left*) the original image, the best-fit model image, and the image of residuals after model subtraction for the g band. (*right*) Isophotal contours of the image, of the model, and of the azimuthal light profile. For clarity, only the model (red line) is over-plotted on the azimuthal light profile, and the (O–C) residuals are shown. Table 4 reports the model parameters. We show 20 isophote levels, between 500 and 2 σ of the sky level ($\mu_g = 21.6 \pm 0.02$ and 26.9 ± 0.34 mag arcsec^{-2} and $\mu_r = 21.0 \pm 0.02$ and 26.6 ± 0.29 mag arcsec^{-2}), for the original and model images. The same panels are shown for the r-band photometry. KIG 264 reveals ripples and tail at the NW side of the galaxy body and a shell system in the outskirts. These features are revealed in both the g and r images above 2σ of the sky level and in the light profiles, starting at $\approx 30''$.

4. Results

Table 4 reports the seeing-corrected parameters derived from the Sérsic and/or the B+D light profile best fit. The table columns are described in the table caption. Columns 12 and 13 report the morphological class we assigned and the notes about the morphology of the residuals after model subtraction. We adopted the following criteria to assign the morphological class: We classified as S0 ($-2 <$ Type ≤ 0) galaxies whose profiles were best fitted by a B+D model and have $0.5 < B/T \leq 0.7$, and we classified as E/S0 (Type $= -3$) galaxies with $0.7 < B/T < 0.8$ (see e.g. Meert et al. 2015, their Fig. 23). Galaxies whose luminosity profile was best fitted by a single Sérsic law (i.e. by definition, $B/T = 1$) were classified as E ($-5 <$ Type < -4). We considered that a nearly pure disc galaxy has a Sérsic index $n \approx 1$ (i.e. by definition, $B/T \approx 0$). We added the notation "pec" to the classification when galaxies have structured residuals.

Uncertainties for the bulge and disc effective radii, ellipticity, and position angles for the adopted models were obtained using the Monte Carlo simulation method. Noise and the uncertainty in the sky level determination were added. The errors on ellipticity, position angle, bulge effective radius, etc. quoted in the table are based on variables that do not depend on the model, in this case, Poisson noise. More realistic errors are likely larger. This can be verified by comparing the values among the bands: the differences may reach 10%, which is common for this type of model fitting.

4.1. Comparison with the literature

In Fig. 6 we compare the difference between our total integrated magnitudes, reported in Table 4, and the g and r bands from SDSS DR16 (Table 2). Our magnitudes are brighter on average by 0.10 and 0.09 mag in g and r bands, respectively. This value is higher than the measurement errors. KIG 637, which is not included in Fig. 6, presents integrated magnitude values that differ largely ($\approx$0.46 mag) from the SDSS DR16 values. The excess

Table 4. KIG photometric data from the adopted Sérsic and B+D best-fit models and morphological notes.

KIG	Filter	$\epsilon_{\rm bulge}$	$\epsilon_{\rm disc}$	$PA_{\rm bulge}$ [deg]	$PA_{\rm disc}$ [deg]	$r_{e,\rm bulge}$ [″]	$r_{\rm scale,disc}$ [″]	n	m_T [ABmag]	B/T	Morphological class	Notes on residual morphology
(1)	(2)	(3)	(4)	(5)	(6)	(7)	(8)	(9)	(10)	(11)	(12)	(13)
264	g	0.65 ± 0.06	0.21 ± 0.03	91.4 ± 1.4	107.8 ± 1.7	1.00 ± 0.10	6.01 ± 0.30	…	14.66 ± 0.03	0.68	S0 pec	NW fan, tail and shells
	r	0.48 ± 0.05	0.13 ± 0.02	92.8 ± 1.4	105.4 ± 1.8	1.25 ± 0.11	7.46 ± 0.30	…	13.83 ± 0.05	0.62		
378	g	0.28 ± 0.03	0.27 ± 0.02	170.3 ± 2.7	166.8 ± 2.6	4.14 ± 0.51	5.36 ± 0.31	…	15.06 ± 0.02	0.63	S0 pec	NW asymmetric residuals (tail?)
	r	0.25 ± 0.02	0.31 ± 0.03	168.8 ± 2.6	165.7 ± 3.9	5.05 ± 0.57	6.17 ± 0.11	…	14.17 ± 0.02	0.78		
412	g	0.14 ± 0.03	0.12 ± 0.02	98.8 ± 1.3	67.9 ± 1.1	3.55 ± 0.45	6.84 ± 2.91	…	15.40 ± 0.03	0.69	E/S0 pec	inner and outer rings, shell-like structures
	r	0.15 ± 0.02	0.11 ± 0.02	95.7 ± 1.5	51.0 ± 1.1	2.86 ± 0.14	8.25 ± 0.63	…	14.53 ± 0.04	0.71		
481	g	0.48 ± 0.05	0.30 ± 0.03	97.0 ± 1.0	81.1 ± 1.0	10.18 ± 0.21	27.12 ± 0.67	…	12.56 ± 0.04*	0.66	S0 pec	dust, concentric shells
	r	0.47 ± 0.05	0.31 ± 0.02	97.1 ± 1.0	81.3 ± 1.0	10.76 ± 0.10	24.81 ± 0.21	…	11.88 ± 0.02*	0.69		
490	g	0.36 ± 0.04	0.17 ± 0.02	33.9 ± 1.4	30.7 ± 1.4	4.21 ± 0.03	8.92 ± 0.42	…	14.39 ± 0.05	0.53	S0 pec	NE plume-tail
	r	0.36 ± 0.02	0.17 ± 0.02	31.5 ± 1.4	34.3 ± 1.5	3.60 ± 0.40	8.55 ± 0.11	…	13.66 ± 0.02	0.50		
517	g	0.29 ± 0.03	0.47 ± 0.03	63.7 ± 1.1	65.5 ± 1.3	4.65 ± 0.20	9.35 ± 0.22	…	14.82 ± 0.12	0.71	E/S0	inner ring, outer irregular residuals
	r	0.21 ± 0.03	0.50 ± 0.04	64.5 ± 1.1	65.1 ± 1.1	3.86 ± 0.10	9.07 ± 0.38	…	14.05 ± 0.09	0.74		
578	g	0.09 ± 0.01	…	78.1 ± 1.5	…	6.86 ± 1.50	…	4.19 ± 0.58	14.96 ± 0.11	…	E pec	inner ring, outer ring or shell
	r	0.10 ± 0.02	…	79.3 ± 1.2	…	6.40 ± 1.60	…	4.18 ± 0.45	14.27 ± 0.02			
595	g	0.41 ± 0.05	0.38 ± 0.03	51.3 ± 1.1	40.1 ± 1.1	20.50 ± 0.21	19.39 ± 2.21	…	14.01 ± 0.05	0.78	E/S0 pec	shells, NW tail at 2σ
	r	0.42 ± 0.04	0.38 ± 0.04	51.5 ± 1.1	40.8 ± 1.1	19.82 ± 0.30	19.82 ± 3.24	…	13.21 ± 0.06	0.78		
599	g	0.24 ± 0.03	0.15 ± 0.02	86.2 ± 1.3	91.3 ± 2.3	2.58 ± 1.19	8.60 ± 1.01	…	14.06 ± 0.06	0.39	S0 pec	shells, spiral arm-like residuals
	r	0.25 ± 0.03	0.15 ± 0.02	89.1 ± 1.3	90.8 ± 2.2	2.48 ± 0.29	8.27 ± 0.29	…	13.29 ± 0.06	0.39		
620	g	…	…	…	…	…	…	…	14.70 ± 0.02		S0	inner ring, disc embedded into halo
	r	…	…	…	…	…	…	…	13.99 ± 0.01			
636	g	0.40 ± 0.04	0.11 ± 0.05	115.8 ± 1.1	171.2 ± 1.7	4.27 ± 0.20	3.91 ± 0.50	…	14.92 ± 0.02	0.74	SB0 pec	inner bar(?), ring, tails or arm-like structures
	r	0.42 ± 0.04	0.10 ± 0.17	116.2 ± 1.1	170.8 ± 1.7	4.79 ± 0.17	3.86 ± 0.25	…	14.21 ± 0.01	0.73		
637	g	0.40 ± 0.04	0.36 ± 0.03	102.7 ± 1.1	99.8 ± 1.1	11.53 ± 0.13	29.64 ± 1.15	…	12.52 ± 0.11	0.56	S0	inner and outer ring
	r	0.40 ± 0.04	0.37 ± 0.05	103.1 ± 1.1	100.4 ± 1.1	10.88 ± 0.15	28.93 ± 1.32	…	11.71 ± 0.11	0.57		
644	g	…	…	…	…	…	…	…	14.74 ± 0.03	…	S0	inner ring and lens
	r	…	…	…	…	…	…	…	13.91 ± 0.02	…		
670	g	0.36 ± 0.03	0.38 ± 0.04	148.9 ± 1.5	148.4 ± 1.3	4.78 ± 0.12	10.91 ± 0.16	…	14.52 ± 0.04	0.72	E/S0 pec	shells, asymmetries
	r	0.36 ± 0.04	0.38 ± 0.03	148.7 ± 1.4	148.8 ± 1.4	4.80 ± 0.11	10.85 ± 0.48	…	13.69 ± 0.01	0.73		
685	g	0.18 ± 0.05	0.16 ± 0.02	99.1 ± 2.5	148.4 ± 1.5	3.55 ± 0.12	7.53 ± 0.60	…	15.31 ± 0.03	0.74	E/S0 pec	shells, rings
	r	0.17 ± 0.05	0.10 ± 0.02	100.2 ± 1.3	150.2 ± 1.3	3.26 ± 0.91	8.33 ± 0.50	…	14.34 ± 0.04	0.65		
705	g	0.01 ± 0.01	…	16.7 ± 2.5	…	3.67 ± 0.12	…	3.61 ± 0.30	14.62 ± 0.05	…	E pec	inner ring, dust ?, shells
	r	0.01 ± 0.01	…	14.7 ± 3.2	…	3.48 ± 0.13	…	4.08 ± 0.48	13.79 ± 0.02	…		
722	g	0.08 ± 0.03	…	96.6 ± 2.0	…	9.33 ± 0.17	…	4.23 ± 0.37	14.13 ± 0.09	…	E pec	shell and fans
	r	0.09 ± 0.03	…	86.2 ± 2.0	…	8.90 ± 0.15	…	3.58 ± 0.39	13.28 ± 0.04	…		
732	g	0.15 ± 0.03	0.04 ± 0.01	61.8 ± 2.0	91.8 ± 2.2	8.18 ± 1.3	13.91 ± 1.78	…	13.11 ± 0.02	0.77	E/S0 pec	shells, spiral arm-like residuals
	r	0.15 ± 0.03	0.01 ± 0.01	64.3 ± 2.2	90.1 ± 1.0	7.95 ± 1.4	13.50 ± 1.45	…	12.43 ± 0.01	0.79		
733	g	…	…	…	…	…	…	…	14.44 ± 0.16	…	S0 pec	open arms, ring
	r	…	…	…	…	…	…	…	13.60 ± 0.14	…		
841	g	0.49 ± 0.04	0.21 ± 0.02	157.4 ± 1.1	148.4 ± 1.1	10.57 ± 1.14	17.45 ± 1.25	…	13.22 ± 0.01*	0.59	S0 pec	dust-lane, shells
	r	0.46 ± 0.05	0.24 ± 0.02	158.5 ± 1.1	148.9 ± 1.1	10.07 ± 1.14	17.47 ± 1.32	…	12.43 ± 0.03*	0.62		

Notes. The elllipticity and position angle for the bulge, ($\epsilon_{\rm bulge}$, $PA_{\rm bulge}$), and disc components, ($\epsilon_{\rm disc}$, PA_{disc}), are given in Cols. 3–6. The bulge, $r_{e,\rm bulge}$, and disc, $r_{\rm scale,disc}$ effective radii and disc scale length, in Cols. 7 and 8, refers to B+D decomposition. When the best fits is obtained with a single Sérsic law fit, whose index n is given in Col. 9, $r_{e,\rm bulge}$, $\epsilon_{\rm bulge}$ and $PA_{\rm bulge}$ refers to the whole galaxy. The value of m_T in Col. 10 refers to the galaxy magnitude from the aperture photometry integration. When the 4K-CCD gap is present, we report the total integrated magnitude of the model (indicated with the asterisk). Column 11 reports the ratio between the bulge and the total flux of the galaxy obtained from the B+D model of the light profile. Column 12 provides the morphological class according to the criteria explained in the first paragraph of Sect. 4. Column 13 summarises the morphology of the residuals after the model subtraction. Detailed comments about the galaxy morphology are given in Sect. 4.2.

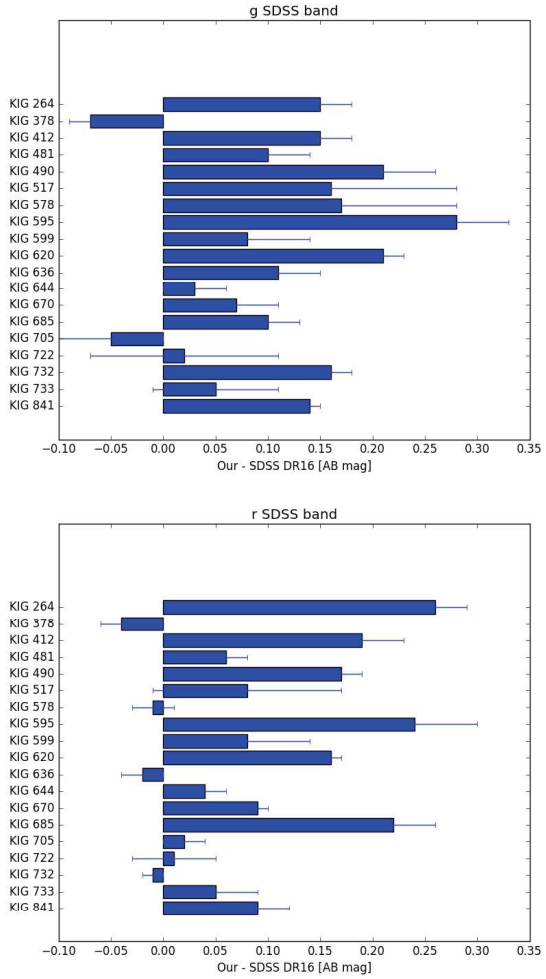

Fig. 6. Comparison between our integrated magnitudes in g and r bands with the SDSS DR16 values reported in Table 2. The solid lines show our errors. KIG 637 is not plotted because the magnitudes are strongly influenced by the nearby bright star HD238370 (see Sect. 4.2).

in magnitude in our measures in this case is partly associated with the diffuse light of HD 238370, a very bright nearby star that cannot be properly modelled and subtracted. The extension of the stellar corona is visible in the top panels of Fig. A.6, showing g and r residuals.

Comparisons with other photometric works and/or recent photometries are difficult for the following reasons: (1) our values refer to either a simple Sérsic law or to a B+D decomposition, that is, they are tied to the adopted model, and (2) our photometry is deeper, for example, than data sets extracted from SDSS images, for instance. The ellipticity, ϵ, and the position angle, PA, of our models are not directly comparable with the values provided in Table 2. We averaged the $g-$ and r-band values of ϵ and of PA for each galaxy. These results are in general comparable with the ϵ and PA data in Table 2. Our PA of the bulge, 102.7 ± 1.1 and 103.1 ± 1.1 in g and r band, and of the disc, 99.8 ± 1.1 and 100.4 ± 1.1, of KIG 637 (NGC 5687) compares well with 103.6 ± 0.01 and 101.2 ± 0.1 provided by the two Sérsic-law fits by Costantin et al. (2018). The same holds for the ellipticity of the bulge, 0.40 ± 0.04 in both bands, and of the disc 0.36 ± 0.03 and 0.37 ± 0.03 in g and r bands compared with 0.314 ± 0.001 and 0.338 ± 0.001 by Costantin et al. (2018).

The parameters of the 2D galaxy model, provided in Table 4, are complemented by Figs. A.1–A.9 in Appendix A. The caption of Fig. 5 details the information provided by the galaxy modelling. Our interest in particular is the detection of the galaxy fine structure, such as stellar tails, streams, fans, and shells. The light-profile fit and the residuals after the 2D model subtraction are shown for each band in the bottom panels of these figures.

The $(g - r)$ colour profiles are collected in Fig. 7. In Fig. 8 the colour profiles are divided into three categories and plotted using a kiloparsec scale in the abscissa. In discussing $(g-r)$ colour profile, we recall that because the flat field is imperfect, we had to fit the background with `SWarp` (Bertin et al. 2002) (see Sect. 3). This might influence the colour profile in the low surface brightness regimes, where the errors are indeed quite large. Outside the seeing region, the trend of the vast majority (see the middle panel) of the colour profiles is flat, with values typical of ETGs, that is, around 0.7–0.8 mag. The colour profiles of KIG 264 and KIG 378 $(g - r)$ are shown in the top panel. They tend to become redder with radius. The bottom panel includes colour profiles either with peculiar trends, such as those of KIG 636 and KIG 841, or profiles that become bluer with radius. Single colour profiles are discussed in Sect. 4.2.

4.2. Individual notes

In this subsection we discuss the results summarised by the figures in Appendix A. Detailed surface photometric studies have been dedicated to some of the iETGs we study here by H-T, Rampazzo et al. (2019) in the K band and by Costantin et al. (2018) in the SDSS i band. Automatic surface photometry and 2D luminosity profile decomposition in these SLOAN bands have also been performed for some objects by Simard et al. (2011) and by Meert et al. (2015). In our discussion of the $(g-r)$ profile, we exclude values with a radius below three times the FWHM, which are perturbed by the seeing, and measurement in the outskirts with errors larger than 0.3 mag.

KIG 264. The galaxy is considered a barred lenticular by Buta et al. (2019) and `HyperLeda` classifications, as a mixed E/S0 by Fernandez-Lorenzo et al. (2012), and as an E by H-T. The fit with a single Sérsic law provides a poor fit of the light profile; a B+D model (see Fig. 5) gives a statistically much better representation. Our surface photometry suggests the presence of a disc, but we did not find evidence of a bar. The cross-like shape in the g and r residuals in the inner regions (see Fig. 5) is an artefact due to the boxy shape of real isophotes with respect to our model. The isophotes boxiness has previously been noted by H-T. In the NW, the SE and NE residuals (Fig. 5) compose a shell structure. A fan, likely a wide tail, starting from the galaxy body, is attached to the NW part of the shell structure. These features have not been detected in the study by H-T. The B+D model fits the luminosity profile well up to the fan that appears as an increase of the disc surface brightness starting at $\approx 30''$ in the g and r bands. The $B/T = 0.68$ in both bands indicates that the bulge component is dominant. We suggest that the galaxy is a peculiar unbarred S0. The $(g - r)$ colour profile grows monotonically from ≈ 0.5 mag to unusually high red values in the galaxy outskirts, which may suggest the presence of dust.

KIG 378. The galaxy is classified as an elliptical by Buta et al. (2019) and `HyperLeda`, but it is considered as an E/S0 by Fernandez-Lorenzo et al. (2012) and as a S0 by H-T. The luminosity profile is statistically best fitted by a B+D model (Fig. A.1). The exponent of the single Sérsic-law fit is $n \approx 3$,